THE STUDY OF THE IMPACT OF ANGULAR MOMENTUM TRANSPORT IN LOW MASS RED GIANT STARS USING ASTEROSEISMOLOGY

Beatriz Bordadágua[1]

[1]*Centro de Astrofísica e Gravitação - CENTRA, Departamento de Física, Instituto Superior Técnico - IST,
Universidade de Lisboa - UL, Av. Rovisco Pais 1, 1049-001 Lisboa, Portugal*

ABSTRACT

Asteroseismic measurements enabled by the *Kepler* mission revealed lower rotation rates of red giant's cores than theoretical predictions, highlighting some gaps in the theory of stellar interiors. We used the Modules for Experiments in Stellar Astrophysics evolution code to compute state-of-the-art models of the *Kepler* target, KIC8579095, from the zero-age main-sequence (ZAMS) to the red giant branch (RGB). We included angular momentum (AM) transport and chemical mixing in radiative zones due to hydrodynamical instabilities, and magnetic fields generated by the Tayler-Spruit dynamo and the recent revision – Fuller-formalism. This last model, was the only one able to best reproduce the observed RGB core rotation. The mixing induced by the Fuller-formalism, computed for the first time in our work, revealed to be very small. Nonetheless, the AM transport efficiency increases with the inclusion of mixing. We also used the pulsation code, GYRE, to further study this mechanisms using asteroseismic observables. Lastly, we tested the efficiency of AM transport of Fuller-formalism models for different input physics. And using a sample of 1093 stars from the main-sequence (MS) to the red clump (RC) phase in the $1 - 2 \, \mathrm{M_\odot}$ range, we found that a wider range for the free parameter $\alpha \in [0.5; 5]$ in the Fuller-formalism is needed to reproduce rotation asteroseismic measurements.

Key words: asteroseismology – stars: structure – stars: rotation – stars: angular momentum – stars: mixing

1. INTRODUCTION

Over the past decade, major improvements in high-resolution spectroscopy and the success of space missions such as CoRoT (Baglin et al. 2007), *Kepler* (Gilliland et al. 2010; Koch et al. 2010), and most recently TESS (Ricker et al. 2014) have significantly increased the number of stars, particularly red giants, with detected nonradial oscillations and the resolution of oscillation patterns.

The pulsation modes identified in stellar surfaces are originated by waves propagating in stellar interiors stochastically excited by convective noise. The simplest normal modes that stars can pulsate in are radial modes, where the star expands and contracts in a periodic motion. In nonradial modes some parts of the star move up while others are going down periodically, changing the stars' shape and breaking spherical symmetry. For radial motion the pressure acts as the main restoring force to small perturbations of the equilibrium position, leading to the formation of the so-called p-modes, whereas for predominately horizontal motion, gravity acts through buoyancy as the restoring force, originating g-modes (e.g., Aerts et al. 2010). After the MS, the core contraction and subsequent envelope expansion leads to an overlap in the frequency domain of p- and g-modes. Hence, nonradial modes develop a mixed nature (predicted theoretically by Dziembowski et al. (1971) and Shibahashi (1979)) exhibiting g-mode behavior in the convectively stable core of the star and p-mode behavior in the outer convection regions. These so-called *mixed modes* have the potential to probe the entire star (e.g., Chaplin et al. 2013).

In that stage, conservation of AM requires the contracting core to spin up and the expanding envelope to spin down (Marques et al. 2013; Deheuvels et al. 2014). *Kepler*'s measurements of rotational splittings of dipole mixed modes have shown red giants cores rotating around ten times faster than the surface (e.g., Mosser et al. 2012), revealing a strong differential rotation profile (Marques et al. 2013). Beck et al. (2012) found lower core rotation in red giants in opposition to model predictions, highlighting some inaccuracies in the current description of internal AM transport. The discovery of g-dominated mixed modes in red giants also provided a clear separation between hydrogen shell burning and helium core burning stars (RC stars) (Bedding et al. 2011). Asteroseismic estimates of RC stars show they are rotating six times slower than red giant cores (Mosser et al. 2012). This can be somewhat explained by the change in core radius during He-burning, but not entirely, suggesting a strong transfer of AM from the inner to outer regions.

There are several mechanisms that try to explain the physics of AM transfer processes in stellar interiors (see an extensive discussion in Aerts et al. (2019)). Some of the most accepted include hydrodynamic instabilities and meriodional circulation, however internal torques generated by this processes are rather ineffective, thus fail to explain the asteroseismic inferred core rotation rates of evolved stars, predicting spins two orders of magnitude higher (e.g., Heger et al. 2000; Cantiello et al. 2014). Internal gravity waves (see Rogers et al. (2013)) and torques due to magnetic fields in radiative zones (e.g., Tayler-Spruit (TS) dynamo by Spruit (2002) or the revised version by Fuller et al. (2019)) are stronger candidates to explain the

transport of AM. However there is still no consensus on which of the two processes above is dominant since both require calibrations of free parameters to reach the inferred asteroseismic rotation rates.

We focus on studying the impact of different prescriptions of AM transport, with emphasis on the Fuller-formalism, in the stellar evolution and structure of low mass RGB stars. Eggenberger et al. (2019c) demonstrated that the Fuller-formalism is more efficient transporting AM in radiative interiors than meriodinal circulations and other hydrodynamic instabilities. The Fuller-formalism is also able to reproduce core rotation rates of low mass SGB, RGB and even RC stars, however recent tests showed that it is not the solely solution for the missing AM problem. Eggenberger et al. (2019a) found that a different value for the free parameter $\alpha = 0.5$ was needed to match the frequency splittings for SGB stars, in contrast with $\alpha = 1.5$ required to RGB stars. For RC stars, denHartogh et al. (2020) argued that α between 2 and 4 was required to match the observations. For white dwarfs (WD) the Fuller-formalism could not match the core rotation rates, unless when it was excluded at the end of the core He-burning phase.

In the following section we present the physical details for AM transport and rotation-induced chemical mixing of the Fuller-formalism. Section 3 describes the computational models and methodology to obtain the results of next section. Section 4 shows the AM evolution of stellar models using four different mechanisms. We incorporate, for the first time, chemical mixing due to the Fuller-formalism, using the coefficient derived by Fuller et al. (2019) (Section 4.1). In Section 4.2 we compute important asteroseismic variables that can be used to extend our knowledge in stellar interiors. Section 5 presents the AM evolution of stellar models using the Fuller-formalism from the ZAMS to the RC phase. We tested the sensibility of the Fuller-formalism to different input parameters (Section 5.1). Using up-to-date asteroseismic inferred rotational splittings, we also found new limits for the α parameter of this formalism (Section 5.2). Our conclusions are summarized in Section 6.

2. TRANSPORT OF ANGULAR MOMENTUM VIA THE FULLER-FORMALISM

In the Spruit (2002) prescription, the stars' latitudinal differential rotation shears an original weak magnetic fossil field generating a toroidal field (B_ϕ) – by the so-called Ω-effect. After a few turns, the toroidal component strength grows and becomes unstable as the first hydrodynamic instability sets in, the Tayler instability (Tayler 1973; Pitts et al. 1985), that can take place in stably stratified regions. This instability will reproduce the radial field (B_r) components necessary to close the loop (by the α-effect). They eventually will be sheared again into a poloidal field, repeating the process so-called TS dynamo.

Spruit (2002) proposes that the energy in the background toroidal field is damped into small scales with a specific rate, i.e., energy dissipation from non-linear effects. At saturation, the energy obtained from winding the radial field equals the energy dissipation rate. The magnetic torque produced via

Maxwell stresses that redistributes the AM is calculated using the $B_r B_\phi$ field strength at saturation.

There are a couple of important aspects on the theoretical basis of this mechanism that have been criticized by Zahn et al. (2007) and Fuller et al. (2019). Nonetheless, the Spruit prescription achieves rotation rates orders of magnitude lower than most mechanisms, and only one order higher than observations (Cantiello et al. 2014).

A revision of this mechanism was performed by Fuller et al. (2019) (recently referred as the Fuller-formalism) which achieves better agreement with observations and addresses the previous theoretical concerns. Fuller et al. (2019) proposed a lower damping rate for the components of the perturbed toroidal field than Spruit (2002), leading to stronger magnetic fields and consequently higher Maxwell torques in the saturated regime. Hence, the Fuller-formalism transports AM more efficiently than the TS dynamo. The associated viscosity coefficient ($\nu = B_r B_\phi / 4\pi\rho q\Omega$) and the minimal shear $\left(q = -\frac{\partial \ln \Omega}{\partial \ln r}\right)$ for the Tayler instability to set in for the Fuller-formalism can be written as

$$\nu_{\mathrm{F}} = \alpha^3 r^2 \Omega \left(\frac{\Omega}{N_{\mathrm{eff}}}\right)^2; \quad q_{\min} = \alpha^{-3} \left(\frac{N_{\mathrm{eff}}}{\Omega}\right)^{5/2} \left(\frac{\eta}{r^2\Omega}\right)^{3/4}.$$

(1)

where α is a dimensionless calibration parameter ($\alpha \sim 1$), N_{eff} is the effective Brunt-Väisälä frequency given by $N_{\mathrm{eff}}^2 = \frac{\eta}{K} N_T^2 + N_\mu^2$, with η and K the magnetic and thermal diffusivities, N_T and N_μ the thermal and chemical composition components.

The small fluid displacement in the radial direction due to the saturation of the Tayler instability is usually orders of magnitude lower than the horizontal displacements, hence a possible generated chemical mixing will be less efficient than the transport of AM. Fuller et al. (2019) estimated the mixing of chemical elements induced by the Tayler instability to be fairly negligible, nonetheless derived the following relation:

$$D_{\mathrm{F}} = \alpha^3 r^2 \Omega \left(\frac{\Omega}{N_{\mathrm{eff}}}\right)^2 \left(\frac{q\Omega}{N_{\mathrm{eff}}}\right)^{5/3}.$$

(2)

3. KIC 8579095: STELLAR MODELS WITH TRANSPORT OF ANGULAR MOMENTUM

Stellar evolution models were computed with the release version 12115 of Modules for Experiments in Stellar Astrophysics (MESA; Paxton et al. 2011; 2013; 2015; 2018; 2019). These models incorporate rotation and the effects of centrifugal force on the stellar structure by adopting the so-called shellular approximation (Zahn 1992; Meynet et al. 1997), where the angular velocity depends very weakly on latitude and is almost constant on isobars ($\Omega \approx \Omega(r)$). All models are set at the ZAMS with initial solid body rotation and spin rate of ~ 3.6 days.

AM transport and the evolution of chemical elements are computed separately using a diffusive approach (Endal et al. 1978; Heger et al. 2000), that can be written as

$$\left(\frac{\partial \Omega}{\partial t}\right)_m = \frac{1}{i}\left(\frac{\partial}{\partial m}\right)_t\left[(4\pi r^2\rho)^2 i\nu\left(\frac{\partial \Omega}{\partial m}\right)_t\right] - \frac{2\Omega}{r}\left(\frac{\partial r}{\partial t}\right)_m\left(\frac{1}{2}\frac{d\ln i}{d\ln r}\right),$$

(3)

$$\left(\frac{\partial X_n}{\partial t}\right)_m = \left(\frac{\partial}{\partial m}\right)_t\left[(4\pi r^2\rho)^2 D\left(\frac{\partial X_n}{\partial m}\right)_t\right] + \left(\frac{dX_n}{dt}\right)_{nuc},$$

(4)

where i is a shell specific moment of inertia, and ν is the turbulent viscosity calculated as the sum of the diffusion coefficients for convection, semiconvection, and rotationally induced instabilities (neglecting interactions such as amplification and damping between some instabilities). X_n is the mass fraction for the n'th nucleus and D is the diffusion coefficient determined as the sum of individual mixing processes.

We calculate four separate models assuming different physics for AM transport and mixing of chemical elements in radiative regions (e.g., different ν and D coefficients in equations (3) and (4)): 1) a model that ensures total conservation of AM between each step of evolution, and does not include stellar wind (or major mass loss) or account for any AM transport or mixing of chemical elements induced by rotation; 2) a model that includes AM transport and rotation-induced mixing ensured by a combination of several hydrodynamical instabilites described in great detail in Heger et al. (2000); 3) a model with transport of AM and mixing according to the TS description (Spruit 2002); and 4) a model with the implementation of the Fuller-formalism for mixing of AM and chemical elements (following the publicly available MESA inlist of Fuller et al. (2019)).

3.1. *Input physics: calibration process*

We selected the rotating RGB star KIC 8579095 with an estimated mass of $1.366\,\mathrm{M}_\odot$, that is a target from the APOKASC catalog (Pinsonneault et al. 2018) and combines general spectroscopic quantities with crucial seismic quantities to model the evolution of a star. The observed and previously estimated parameters are summarized in table 1.

We took advantage of the *astero* module (Paxton et al. 2013) incorporated in MESA, to generate calibrated models from the ZAMS to the current day (allowing a direct comparison with current observations) of KIC 8579095. The stellar model calibration process takes as inputs parameters $\{\mathrm{M_{ini}}, \mathrm{Y_{ini}}, \mathrm{[Fe/H]_{ini}}, \alpha_{\mathrm{MLT}}, f_{\mathrm{ov}}\}$ and, throughout the stellar evolution, at each timestep, performs a comparison to the chosen observational constraints $\{\mathrm{T_{eff}}, \log g, \Delta\nu\}$, computing a χ^2_{star} value.

The χ^2_{star} value is calculated by weighting the contribution of spectroscopic χ^2_{spec} and seismic χ^2_{seis} observable according to $\chi^2_{star} = 2/3\chi^2_{spec} + 1/3\chi^2_{seis}$ with

$$\chi^2_{spec/seis} = \frac{1}{N}\sum_{i=1}^{N}\left(\frac{X_i^{mod} - X_i^{obs}}{\sigma_{X_i}}\right)^2$$

(5)

where N is the number of parameters, X_i^{mod} and X_i^{obs} are the stellar model and observed values of the ith parameter, respectively, with σ_{X_i} being the observational uncertainty.

Quantities	Values	Sources
$\mathrm{T_{eff}}$ (K)	4773.6 ± 72.9	Abolfathi et al. (2017)
[Fe/H]	0.352 ± 0.025	Abolfathi et al. (2017)
$\log g$ (seis)	3.091 ± 0.005	Pinsonneault et al. (2018)
M ($\mathrm{M}_\odot$)	1.366 ± 0.039	Pinsonneault et al. (2018)
R ($\mathrm{R}_\odot$)	5.512 ± 0.014	Pinsonneault et al. (2018)
$\nu_{\max}$ (μHz)	152.046 ± 0.009	Pinsonneault et al. (2018)
	152.46	Gehan et al. (2018)
$\Delta\nu$ (μHz)	11.942 ± 0.004	Pinsonneault et al. (2018)
	12.0	Gehan et al. (2018)
$\Delta\Pi_1$ (s)	77.9 ± 0.92	Vrard et al. (2016)
	78.2	Gehan et al. (2018)
$\delta\nu_{\mathrm{rot}}$ (nHz)	285.0 ± 1.46	Gehan et al. (2018)

Table 1. Observed and estimated parameters of KIC 8579095. The illustrated columns correspond to: effective temperature, metallicity, log of asteroseismic surface gravity, stellar mass, stellar radius, frequency of maximum power, large frequency separation, dipole mode period spacing, rotational splitting frequency.

To determine the optimal set of input parameters (minimum χ^2_{star}) an optimization run is performed using the Nelder-Mead simplex algorithm (Nelder et al. 1965) implemented in the *astero* module. For each MESA simulation, the *astero* module is called at each timestep to calculate the χ^2_{star} values from the current MESA model output parameters. This process is repeated multiple times with a different set of inputs until several models, with reasonable χ^2_{star} value, have been found. We selected the model with the minimal χ^2_{star} and use it as our benchmark model (see input parameters in Table 2).

$\mathrm{M_{ini}}$ ($\mathrm{M}_\odot$)	$\mathrm{Y_{ini}}$	$\mathrm{[Fe/H]_{ini}}$	α_{MLT}	f_{ov}
1.405	0.298	0.373	2.04	0.014

Table 2. Input parameters of the benchmark model. The illustrated columns correspond to: initial mass, initial helium abundance, initial metallicity, mixing-length parameter and overshooting parameter.

The benchmark model was computed using the Fuller-formalism prescription described above. The rest of the models with different mechanisms of transport of AM and mixing – AM conservation, hydrodynamic instabilities and TS dynamo – were initialized with the same values of input parameters displayed in table 2. Tables 3 and 4 summarize the properties of the final converged models with the respective χ^2_{star}, without and with mixing of chemical elements, respectively. We notice that the predictions of all these models are compatible with the stellar observational parameters shown in table 1.

3.2. *Asteroseismic diagnostic tools*

For high radial order, there is an asymptotic relation for pure acoustic modes that predicts approximately equally spacing $\Delta\nu$ in frequency (Tassoul 1980). The large frequency separation $\Delta\nu$ is very sensitive to the sound speed $c(r)$ on the

Model	age	M	R	$T_{\rm eff}$	$\log g$	$\Omega_{\rm surf}/2\pi$	$\Omega_{\rm core}/2\pi$	$\Delta\nu$	$\Delta\Pi_1$	$\nu_{\rm max}$	χ^2_{star}
	(Gyr)	(M$_\odot$)	(R$_\odot$)	(K)		(nHz)	(nHz)	(μHz)	(s)	(μHz)	
AM conservation	4.57	1.405	5.640	4753.9	3.083	84	410,327	11.940	79.3	150.91	0.586
Hydrodynamic inst.	4.57	1.403	5.635	4753.8	3.083	84	402,812	11.948	79.4	150.98	1.117
TS dynamo	4.57	1.403	5.637	4753.5	3.083	85	21,824	11.942	79.4	150.88	0.482
Fuller-form. (α=1)	4.57	1.403	5.636	4753.6	3.083	85	1,076	11.943	79.4	150.90	0.496
Fuller-form. (α=1.65)	4.57	1.403	5.637	4753.6	3.083	85	674	11.942	79.4	150.89	0.478

Table 3. Properties of the KIC 8579095 converged RGB models without mixing of chemical elements. The 5 models were computed using the input parameters of table 2. The illustrated columns correspond to: age, mass, radius, effective temperature, logarithm of surface gravity, average surface rotation, average core rotation, large frequency separation for radial modes from scaling relations, dipole mode period spacing, frequency of maximum power from scaling relations.

Model	age	M	R	$T_{\rm eff}$	$\log g$	$\Omega_{\rm surf}/2\pi$	$\Omega_{\rm core}/2\pi$	$\Delta\nu$	$\Delta\Pi_1$	$\nu_{\rm max}$	χ^2_{star}
	(Gyr)	(M$_\odot$)	(R$_\odot$)	(K)		(nHz)	(nHz)	(μHz)	(s)	(μHz)	
Hydrodynamic inst.	4.60	1.403	5.608	4755.98	3.087	85	323,206	12.034	79.5	152.40	176.26
TS dynamo	4.58	1.403	5.633	4754.30	3.083	85	13,112	11.954	79.2	151.08	3.45
Fuller-form. (α=1.65)	4.58	1.403	5.636	4754.03	3.083	85	597	11.943	79.1	150.90	0.50

Table 4. Properties of the KIC 8579095 converged RGB models with rotation-induced mixing of chemical elements. The 3 models were computed using the input parameters of table 2. The illustrated columns are the same as table 3.

outer regions, hence it can be used to estimate the propagation time of sound waves across the star,

$$\Delta\nu = \nu_{nl} - \nu_{n-1\,l} \simeq \left(2\int_0^R \frac{dr}{c(r)}\right)^{-1} . \qquad (6)$$

where ν_{nl} corresponds to the mode frequency of the mode with radial order n and spherical degree l, r is the radial coordinate, and R is the radius at the surface.

The frequency pattern for high-order g-modes in the inner radiative region can be obtain from the asymptotic approximation for a non-rotating star resulting in a spectrum nearly uniformly spaced in period satisfying the following relation by Tassoul (1980):

$$\Delta\Pi_l = \frac{2\pi^2}{\sqrt{l(l+1)}}\left(\int_{r_1}^{r_2}\frac{N}{r}dr\right)^{-1} , \qquad (7)$$

where N is the Brunt-Väisäla frequency. Due to the mixed nature in evolved stars, the period spacing of oscillation modes suffers a departure from asymptotic predictions. Hundreds of stars in *Kepler* data showed decreasing $\Delta\Pi$ with increasing mode period, revealing a "tilted" pattern (e.g., see Aerts (2021)). These slope is a consequence of the star rotation.

In the absence of rotation, frequency modes of different m values are degenerate due to spherically symmetry. In rotating stars, the Coriolis force lifts this degeneracy, and modes with different m split into $2l+1$ frequency components. In slowly rotating stars, where the rotation frequency is well below the oscillation frequencies $2\Omega/\omega \ll 1$, the Coriolis force can be treated as a small perturbation in the equations of adiabatic stellar oscillations (e.g., Aerts 2021),

$$\omega_{nlm} = \omega_{nl0} + m\,\delta\omega_{nlm} , \qquad (8)$$

where ω_{nl0} is the frequency in the nonrotating case. The first-order rotational splitting is given by

$$\delta\omega_{nml} = m\beta_{nl}\int_0^R K_{nl}(r)\Omega(r)dr , \qquad (9)$$

(Aerts et al. 2010) where K_{nl} and β_{nl} are the rotational kernels of the modes that depend on the equilibrium structure of the star and on the mode eigenfunctions (radial and horizontal displacement amplitude functions).

To fully understand the repercussions of the different mechanisms of transport of AM and mixing in the stellar interior we need to investigate the oscillation frequencies and respective eigenfunctions in the crucial regions of the previous obtained MESA stellar models. The oscillation modes and corresponding rotational kernels were obtained using the open source pulsation code GYRE (Townsend et al. 2013; 2018) given the MESA input stellar models (TS dynamo and Fuller-formalism) described above. GYRE was used to compute the oscillation frequencies by solving the fourth-order system of adiabatic equations (e.g., Aerts 2021). Differential rotation is implemented according to the Ω distribution of the equilibrium stellar model (assuming shellular rotation). We took advantage of the lowest-order rotation effects in the oscillations equations included in GYRE (does not account for the Coriolis effects).

4. KIC 8579095: IMPACT OF ROTATION IN STELLAR MODELS

We successfully modeled the stellar evolution of the star KIC8579095 (see Section 3 for the models and its input parameters), reaching the values for measured and estimated quantities $T_{\rm eff}$, $\log g$, $\Delta\nu$, and matching the core rotation rate of the
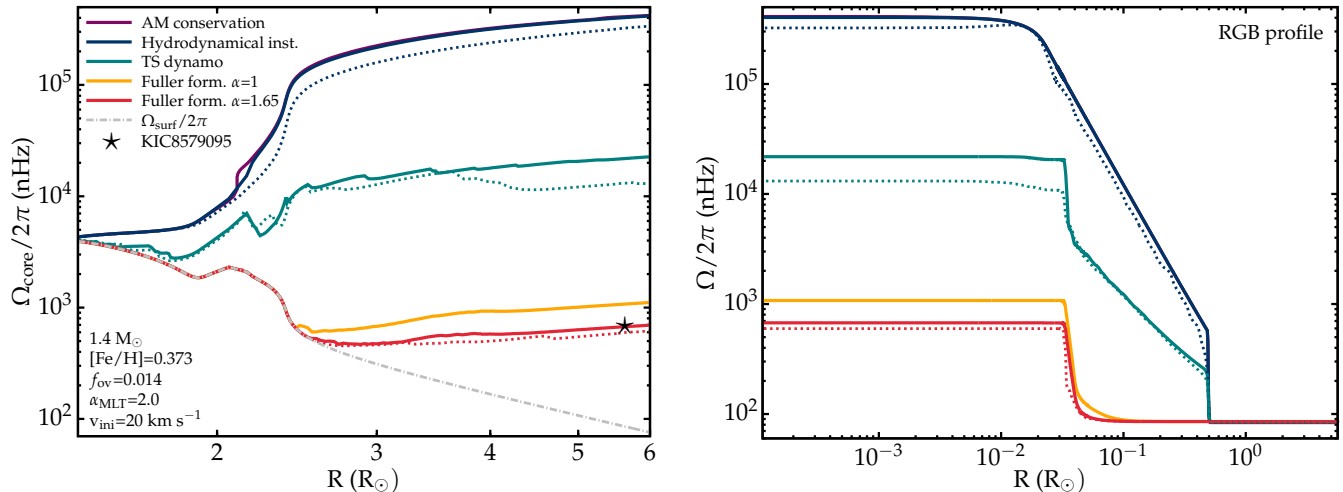
Figure 1. Evolution of core rotation rates as a function of radius from the ZAMS to below the RGB bump (left panel). Rotation profile for calibrated RGB models (right panel). The full (dotted) lines indicate the models without (with) mixing of chemical elements induced by rotation. Models accounting for conservation of local AM (purple), including transport of AM due to hydrodynamic instabilities (blue), and to magnetic torques in radiative regions, with the TS dynamo (green) and with the Fuller-formalism: $\alpha = 1$ (yellow) and $\alpha = 1.65$ (red). The star symbol represents the location of KIC8579095. The grey dashed and dotted line corresponds to the surface rotation rate of all the models.

red giant model to the asteroseismic derived rotational splitting by adjusting the α parameter of the Fuller-formalism.

The models with different mechanisms of transport of AM (figure 1 filled lines, without rotation-induced chemical mixing) barely show any deviations from the point of view of the surface stellar variables (e.g., luminosity, effective temperature, surface gravity), less than 0.05% deviation, and also the asteroseismic diagnostic variables (e.g., large frequency separation, dipole modes period spacing), less than 0.1% deviation. Hence, the significant impact of these mechanisms rely on the evolution of the core rotation rates and they solely differ in the efficiency of transport of AM from the inner to outer regions of the star. The mechanisms diverge and predict different core spin rates in the SGB where occurs an internal AM redistribution. On the other hand, the surface rotation behavior is similar for all models, and evolves as rigid rotation throughout all stages of evolution.

The model accounting for conservation of AM (purple) predicts the highest core rotation rates at all times, and a core spin up of more than 2 orders of magnitude higher than observed values for this red giant (see left panel of Figure 1). This model has no substantial mass loss star, thus in the MS phase the model does not lose mass and already spins faster comparing to the other models. In the SGB, due to the local conservation of AM, the core contracts and spins up drastically while the surface expands and consequently spins down to very low values. Along the RGB, the core continues to spin up but at a lower rate, and the surface continually spins down.

The inclusion of transport of AM through hydrodynamical instabilities (blue) also leads to higher core rotation rates in the RGB than current measurements. In fact this model predicts almost the same rotation rate as the model with conservation of AM, which reveals how non efficient this mechanisms are in this mass range.

The TS dynamo model (green) provides a lower core spin up at the SGB than the model considering local conservation of AM or with hydrodynamic instabilities. However the core rotation rate is still one order of magnitude higher than asteroseismic values. Cantiello et al. (2014) increased the coefficient of diffusion by a factor of 100 however that still did not lower the rotation rate to match observed values.

After the initial spin up in the SGB, the efficiency of transport of AM in the Fuller-formalism (Fuller et al. 2019) model (red and orange) matches the observed core rotation in the RGB. Figure 1 shows 2 models with a different value for the free parameter α of this mechanism. The original paper suggests that $\alpha \approx 1$ is in agreement with asteroseismic core measurements. In our models, a higher value of $\alpha = 1.65$ was needed to meet the core rotation rate of KIC8579095. This parameter enters in the calculation of the viscosity coefficient and in the instability condition and we discuss its implications in the Section 5.

The left panel of Figure 1 illustrates the rotation profile of the RGB calibrated models, for the four mechanisms of transport of AM. All models predict almost rigid rotation in the helium core. The decay of rotation in transition zone between radiative and convective layers, with H-burning in the shell surrounding the core, diverges between models. The conservation of AM, hydrodynamical instabilities and the TS dynamo models decay exponentially (as can be seen in figure 1). Whereas the Fuller-formalism decays with a $\tanh(r)$ function (as implemented in the code from Fuller et al. (2019)). In the convective zones, all the models show almost uniform rotation.

4.1. *Rotation-induced chemical mixing*

Mixing of nuclides modifies the elements stratification in the inner regions, and in particular, rotation-induced mixing is known to affect the evolutionary tracks in the HR dia-
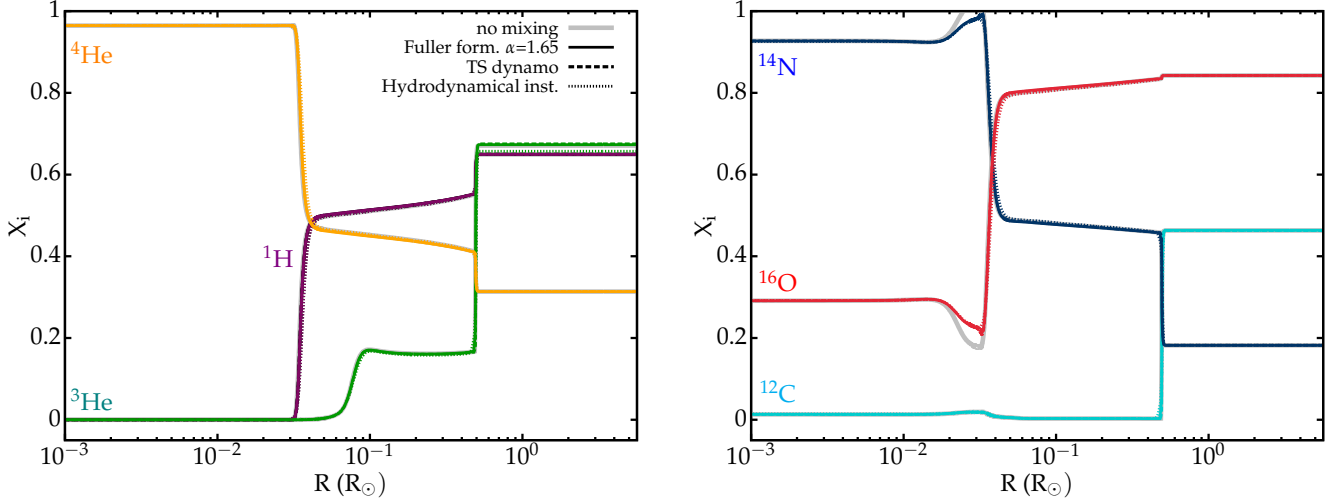
Figure 2. Evolution of mass fractions of several chemical species with radius for KIC8579095 model. In the top panel the mass fractions are ^{1}H (purple), ^{4}He (yellow) and multiplied by 1000 ^{3}He (green). In the bottom panel the mass fractions are multiplied by 50 for ^{12}C (green), ^{14}N (blue) and multiplied by 100 for ^{16}O (red). The models without mixing are grey and the models with mixing induced by the hydrodynamic instabilities are the dotted dashed lines, by the TS dynamo mechanism the dashed lines and by the Fuller-formalism the full lines.

gram (Maeder et al. 2000). During the MS phase, new hydrogen (H) is brought into the core and the produced helium (He) transported outwards. As a consequence, evolutionary tracks evolve with more luminosity and effective temperatures, larger helium cores, and extended lifetimes during core burning phases. In the RGB of low to intermediate mass stars, the convective envelope expands and penetrates deeper into the regions where nuclear reactions have altered the chemical composition, and some of these material is transported to the surface (e.g.,Aerts 2021).

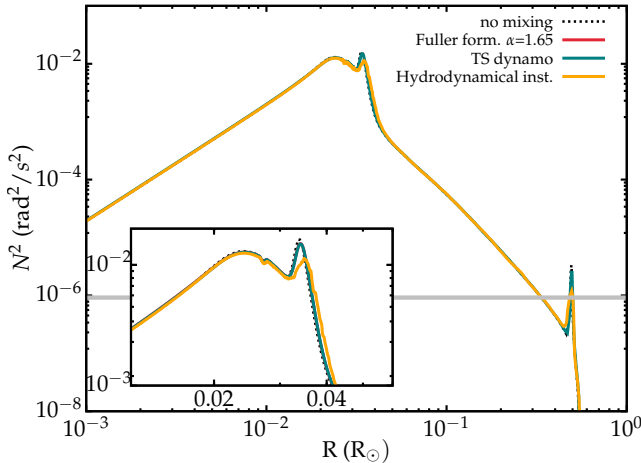The transport of AM mechanisms described above constitute the source of rotationally driven mixing, that transports

Figure 3. Brunt-Väisälä frequency as a function of radius for the RGB models with mixing induced by the hydrodynamic instabilities (yellow), by the TS dynamo mechanism (green) and by the Fuller-formalism (red). The model without mixing is illustrated with a black dashed line. The horizontal grey line indicates the measured frequency of maximum oscillation power ν_{max} of KIC8579095.

chemical elements between layers in stellar interiors. Thus, the detection of surface chemical abundances can indirectly probe the AM missing processes. In this section we included rotation-induced mixing processes (dashed lines in Figure 1) in three of the models of the previous section: hydrodynamic instibilities, TS dynamo and Fuller-formalism (see Table 4).

We calculated that the mixing diffusion coefficient for the model including hydrodynamical instabilities surpasses by 4 and 6 orders of magnitude the coefficient for mixing induced by the TS dynamo and Fuller-formalism, respectively. The expression derived by Fuller et al. (2019) for the mixing of chemical elements (equation (2)) predicts very lower values ($\nu_{\mathrm{mix}}/\nu_{\mathrm{AM}} \sim 10^{-6}$). This hypothesis was not previously tested in computational models, hence we implement this expression in our models for the first time to test the statements of the original paper. We observed that $\nu_{\mathrm{mix}}/\nu_{\mathrm{AM}}$ varies from 10^{-13} to 10^{-5} in the regions where the instability is triggered. Manifesting slightly higher mixing than what was initially theorized, nonetheless still very low values and non significant. However, the resolution of this processes in numerical evolution codes needs to be improved in order to derive further conclusions.

The repercussions in the internal properties of the star due to rotation-induced mixing are more visible in the asteroseismic variables (e.g., large frequency separation and mixed mode period spacing; see tables 3 and 4). There are small but visible changes in the density and abundance profile in the RGB model due to the mixing processes (see figure 2). In figure 1 we can identify that models including rotation-induced mixing predict slightly lower rotation rates. The induced mixing seems to act as an additional AM diffusion coefficient increasing its transport efficiency.

The Brunt-Väisälä frequency (figure 3) is also affected due to the change in compositional gradient in the inner layers (below the convective envelope). The highlighted spike around
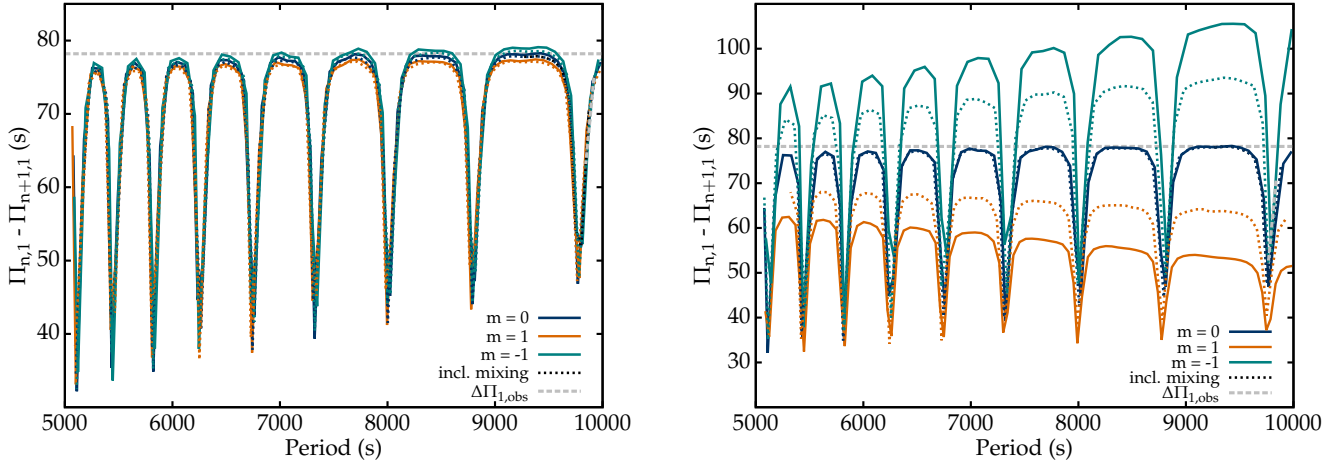
Figure 4. Period spacing of dipole modes as a function of the mode period, for models including the Fuller-formalism (left) and the TS dynamo (right). The grey dashed line represents the estimated dipole mode period spacing $\Delta\Pi_1 = 78.2$ s from Gehan et al. (2018).

0.04 $R_\odot$ that results from a variation in the chemical composition at the H-shell burning displays some disparity between different mixing processes. Nonetheless, this spike is far from the observational window centered around the frequency of maximum oscillation power, so it will unlikely contribute to constraint the mixing coefficients. The second spike around 0.5 $R_\odot$ results from chemical discontinuities left behind by the receding convective envelope. This is the signature of the first dredge up that occurs when a low mass star enters the RGB, where the convective envelope extends up to the nuclear reactions region. There are slight visible differences between mixing mechanisms in that spike, although still not significant. Nonetheless, in more extreme cases (e.g., more efficient mixing mechanisms), this sharp features may affect g-dominated modes (through buoyancy glitches Cunha et al. (2015)) and hence become mensurable.

Models with mixing induced by hydrodynamic instabilities show a less steeper slope (very small difference) than the other models in the tachocline region in Figure 2. Hence, rotation-induced mixing seems to smooth the abundance profile in the interior (also observed in Charbonnel et al. (2010)). Our models do not predict significant modifications in the surface abundances, which can potentially come from the weak mixing power of this rotation-induced mechanisms. However this is an important tracer in order to compare this models with current spectroscopic abundance measurements (Somers et al. (2016)).

Both the mixing of chemical elements by the TS prescription and by the Fuller-formalism show a small effect in Figures 3 and 2 (as expected by Maeder et al. (2004) for the case of TS dynamo). The mixing due to hydrodynamic instabilities has the higher impact as expected.

4.2. *Seismic Analysis of the models*

In this section, stellar oscillations for theoretical models were computed using GYRE (see chapter 3 for details).

The pattern of period spacing in Figure 4 shows mixed modes, predominantly of g-mode character. The several local minima and maxima of the period spacing, suggests that the modes in between those regions are being subject to trapping. At high frequency (low period), the period spacing shows a characteristic decrease as more local minima appear in the pattern due to an increase in p-mode character. At relatively low frequency (high period), the frequency spacing becomes nearly constant in agreement with the asymptotic period spacing (Equation (7); horizontal grey dashed line).

The chemical discontinuities previously described in the Brunt-Väisälä frequency, can also be observed through sharp features (also called glitches) in the oscillation spectrum and in the mixed mode period spacing (Cunha et al. (2015)). We do not observe glitches in the models with mixing which is another possible indication that the impact of this rotation-induced mixing processes is not enough to leave a detectable imprint on oscillation frequencies.

4.2.1. *Rotational splittings*

In Figure 4 it is evident the drastic impact of rotation in the oscillation frequencies. Rotational splittings of g-dominated modes are a great tool to probe the rotation of the central region. Rotation causes a slope on the period spacing pattern in the low frequency g-dominated modes, and higher rotations lead to steeper slopes. The splitting of oscillation frequencies increases with the higher rotation rates, hence models with TS dynamo mechanism predict higher splittings. On the other hand, in the previous section we observed that including rotation-induced chemical mixing slightly decreases the core rotation rate, and as we can see in Figure 4, this reflects on a slightly lower frequency splitting.

Overall the variations between models with and without mixing are of very lower amplitudes hence they unlikely will be mensurable. Nonetheless, the potential of asteroseismic diagnostic tools to probe the mixing in stellar interiors should not be dismissed and instead explored with other more efficient mixing processes.

5. ASTEROSEISMIC CONSTRAINTS ON ANGULAR MOMENTUM TRANSPORT MODELS

To estimate how the core rotation period varies with the stellar radius along the SGB, RGB and RC phase we performed a linear fit to logarithm of the data from a sample with 1,093 stars (see Figure 5) and compare the results with the values in Mosser et al. (2012). We found no correlation between the core rotation periods and the stellar mass of the stars in the SGB, RGB and in the RC phase.

During core H-burning, the radius of MS stars does not increase significantly, hence the rotation period does not depend strongly on the radius as we can see from the data in Figure 5. On the SGB, we observe that the period decreases with increasing radius, in opposition to what vanSaders et al. (2013) found. However, the number of subgiant stars in Figure 5 is not enough to take plausible conclusions. From the RGB power law, we found that red giants period slightly increases with radius. We estimate a less steeper slope than found by Mosser et al. (2012) ($P_{RGB} \sim R^{0.7\pm0.3}$), that can possibility be justified by our broader mass range [1,2 $M_\odot$]. RC stars spin down faster as they evolve. The slope found for RC stars agrees with the Mosser et al. (2012).

5.1. *Impact of input parameters in rotation*

To investigate the dependence on the input physics of stellar models on the evolution from the MS to above the RGB bump, when including the Fuller-formalism, several models were generated with different initial stellar masses, metallicities, convective overshooting and α parameters. The benchmark model (purple) was computed with an initial mass of 1.5 $M_\odot$, Z= 0.02, $f_{ov} = 0.015$ and $\alpha_{mlt} = 2$ with an initial period of 2 days and $\alpha = 1$. This mass is commonly used for studying rotating red giants (see e.g., Cantiello et al. 2014). The implementation of AM transport follows the prescription of Fuller et al. (2019).

5.1.1. *Mass*

In the top left panel of Figure 6 we show the evolution of core and surface rotation rates of models with initial masses ranging between 1-2 $M_\odot$, starting from the ZAMS and ending above the RGB bump.

An increase in the mass leads to a decrease in the core rotation rate, and this is particularly notorious at the end of the SGB. The surface rotation rate also decreases with mass, however the difference is less significant than in the core. This behavior is expected according to equation (1) as $\nu_F \sim R^2$. Since more massive stars have higher radius models, they have more efficient AM transport that translates into a decrease in core rotation. Lastly, we observe that the degree of differential rotation in the models increases slowly with mass from the end of the SGB.

5.1.2. *Metallicity*

The major differences in core rotation rates due to initial composition lay in the MS and SGB (see top right panel of Figure 6). The lower metallicity models show shorter total
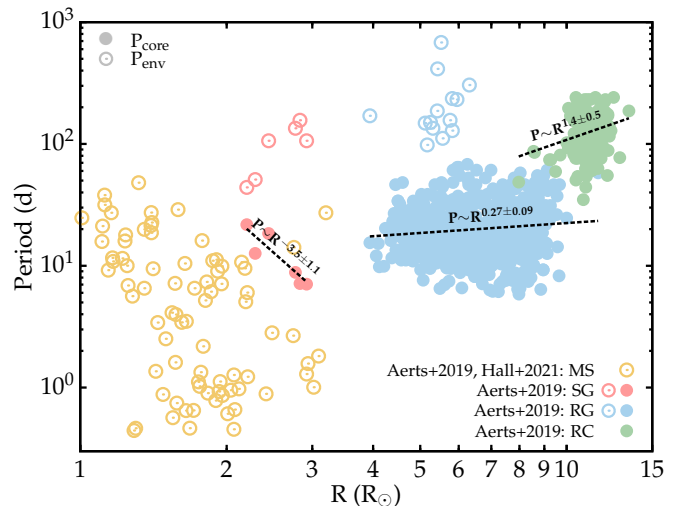

Figure 5. Core (filled circles) and envelope/surface (empty circles) rotation period as a function of the stellar radius for 1,093 stars with masses between 1-2 $M_\odot$. The rotation asteroseismic estimates were taken from Aerts et al. (2019), from Hall et al. (2021) and the respective radius from Aguirre et al. (2017). The dashed black lines indicate the fit performed to SGB, RGB and RC core rotation period. The uncertainties are smaller than the symbol size.

lifetimes. At the end of SGB, the lower metallicity models reach higher helium core radius, which according to equation (1) translates roughly into higher viscosity and more efficient transport of AM to the outer layers, thus lower rotation rates.

As the star moves along the RGB branch this situation is inverted. The more metal rich stars expand more than the metal poor ones (as seen in vanSaders et al. (2013)), thus increasing the efficiency of transport of AM in their cores and consequently slowing them down. Despite the metal rich models reaching higher rotations in the initial stages of evolution, in the late stages they have slowed down and met the rotation rates of the metal poor ones. The top right panel of Figure 6 shows that the core rotation of different metallicity models is almost unaffected in the RGB while surface rotation rates are visibly affected, since metal rich models reach higher surface rotation rates.

5.1.3. *Convective overshooting*

The overshooting parameter f_{ov} is a scaling parameter implemented via a convective diffusion coefficient exponentially decaying beyond the boundary of convection regions. When reduced to zero makes the boundary between the radiative interior and the outer convective zone in stellar models extremely sharp. We tested a range between $f_{ov} = 0 - 0.04$ (as in Paxton et al. (2013)) to understand the impact this parameter has in the rotation rate of models with the Fuller-formalism (see bottom left panel of Figure 6). Increasing overshooting affects the stellar models similarly as increasing initial masses but with more emphasis in the RGB, improving the efficiency of internal transport of AM. The impact on the surface rotation rate of these models is negligible.
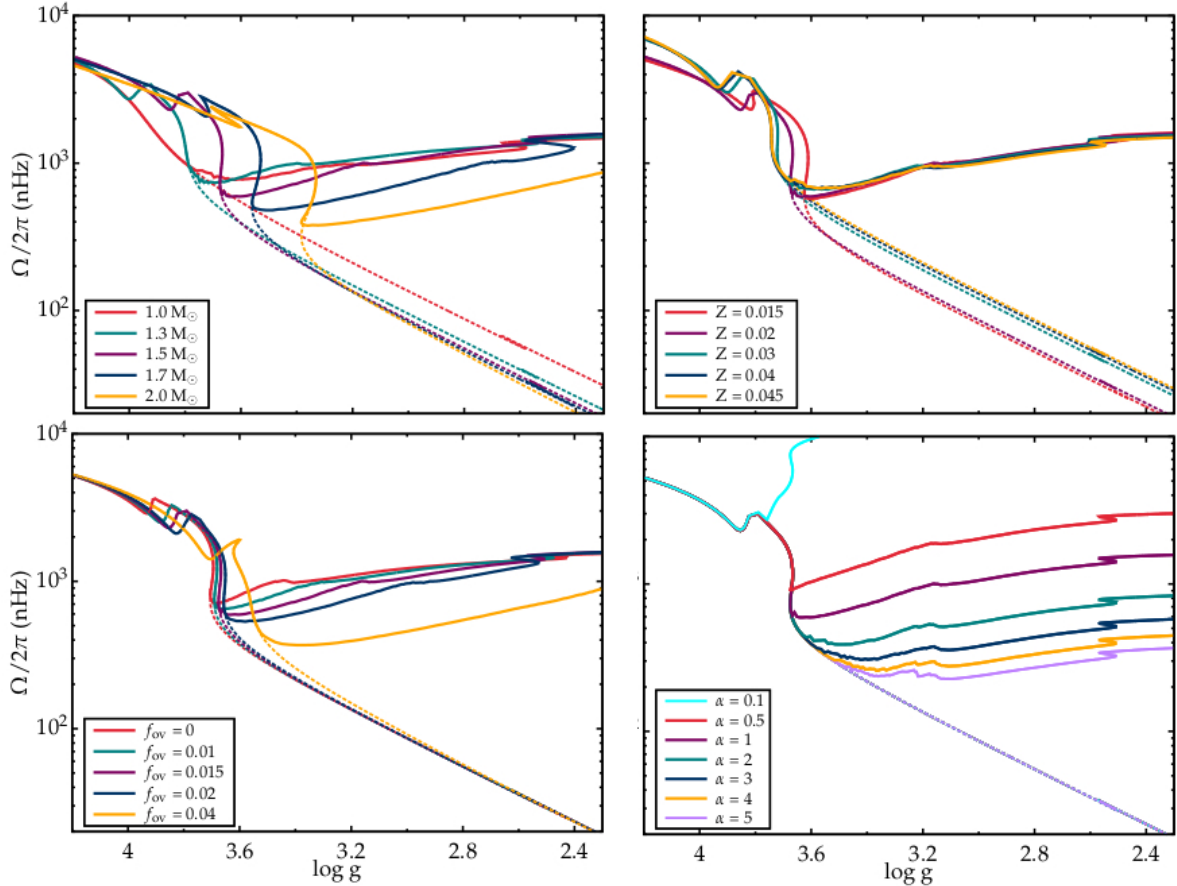
Figure 6. Rotation rates as a function of the surface gravity. The full (dashed) line indicates the core (surface) rotation models. The benchmark model is marked in purple. Top left panel illustrates models with different masses ranging between 1-2 $M_\odot$. Top right panel with different metallicities between $Z = 0.015$-0.045. Bottom left panel with different overshooting parameters between f_{ov} = 0-0.04. Bottom right panel with different α parameter values between $\alpha = 0.1$-5. The input physics of the stellar models is described in the text.

5.1.4. α parameter

The efficiency of transport of AM relies in the coefficient of equation (1). An increase in α enhances the efficiency of transport and core spin down, since $\nu_F \propto \alpha^3$. According to Fuller et al. (2019), the α parameter has an even more significant impact in the computation of the minimum shear $q_{min} \propto \alpha^{-3}$ for the instability to occur. α leads to a decrease in q_{min}, so when $q > q_{min}$, efficient AM transport will tend to decrease the shear until $q \sim q_{min}$ and consequently the reduce the core rotation. The minimum shear in Equation (1) also shows a dependence on the effective Brunt-Väissälä frequency. The shear is strongest where the compositional component N_μ^2 is large due to stratification, and that is at the H-burning shell in the SGB and RGB. As such, we expect the mechanism to be more effective in those phases.

As expected, Figure 6 reveals a significant impact in the core rotation rate in the SGB and RGB with increasing α parameter, and none at the MS where the models experience solid body rotation. The age at which the spin up of the core happens suffers a delay with the increase of α. Higher efficiency of transport of AM prevents the spin up of the core: with a lower α the core spins up during the SGB whereas with a higher α the core only spins up in the early RGB. In the RGB the core

rotation rate decreases up to an order in magnitude $\Omega_{core} \in [200 - 2000 nHz]$ with increase α. The surface rotation rates are unaffected by this parameter. Hence, the models with faster core rotation (e.g., $\alpha = 0.5$) develop a higher degree of radial differential rotation.

5.2. Constraining the α parameter

Using the asteroseismic data from Figure 5 that contains a broader range of core and surface rotation rates of MS, SGB, RGB, and RC stars than Fuller et al. (2019), we establish new limits for the α parameter. To do so, we build two models: one that aims to reproduce the core and surface rotation rate of fast rotators (fast track) and a second for slow rotators (slow track), using the Fuller-formalism. To achieve this, we created two sets of models: in the first set (left panel of Figure 7), the initial rotation period P_i for the fast and slow track models (green and purple) was fixed to match the maximum and minimum observed rotation rates of MS stars. In the second set (right panel of Figure 7), P_i for the fast and slow track models (blue and orange) was allowed to vary. In both sets, the α parameter was chosen to match the core rotation rates of SGB, RGB, and RC stars. All models in Figure 7 were computed with an initial mass of 1.5 $M_\odot$, Z= 0.02, $f_{ov} = 0.015$ and $\alpha_{mlt} = 2$, the rest of parameters are the same as in Fuller et al. (2019).
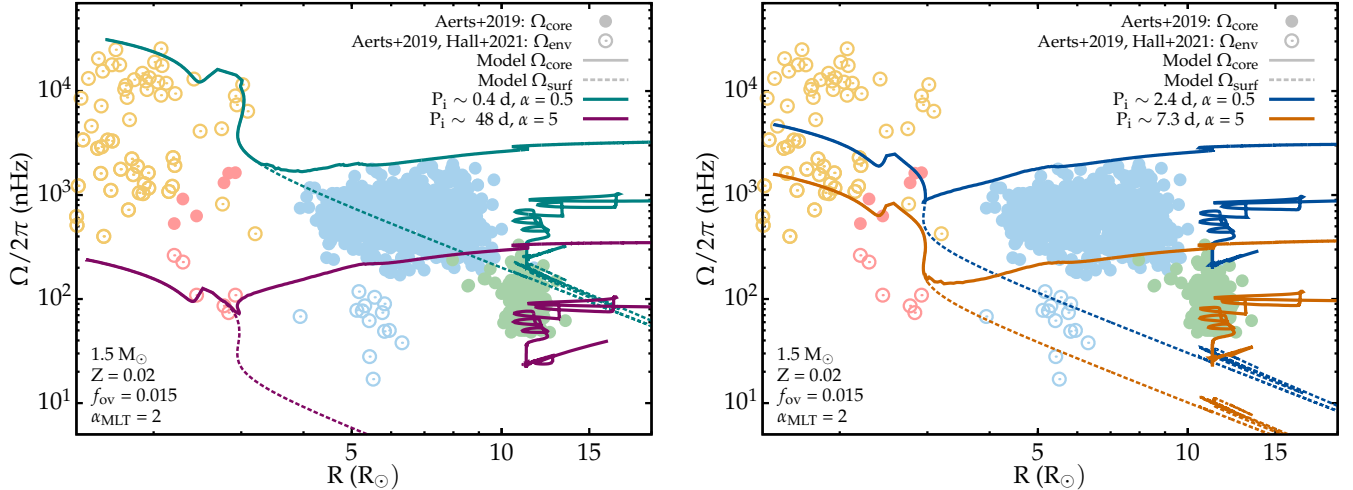
Figure 7. Core and surface (solid and dashed lines) rotation rates as a function of stellar radius from the ZAMS until RC phase. Left panel: models constraining the initial periods of the models to match the MS fastest and slowest rotators. Right panel: models where the initial period was not constrained. The data points are the same as in figure 5.

The lower amount of SGB stars in Figure 7 does not give a good representation of the core and surface rotation rates, mass and metallicity of those stars. More asteroseismic data is needed to fully determine their range of rotation rates and constrain stellar models. The same principle applies to the MS stars in this discussion, as they are sparsely distributed in Figure 7.

For the two sets of models in Figure 7 we obtained the same α parameter values for the fast and slow tracks $\alpha = 0.5$ and $\alpha = 5$, respectively. $\alpha = 0.5$ is needed to model the SGB, RGB and RC fast rotators. At least $\alpha = 5$ is needed to model the slow rotators in the RGB and RC phase. However, even this α value is not enough to reach the lowest core rotation rates. Increasing the α even more shows small to no improvement in slowing down the core, as can be seen in the right panel of Figure 6. Increasing the mass or the convective overshooting would however reach the desired results, hence we defined the limit to be $\alpha = 5$.

Models with the same α converge to the same core rotation rates in the RGB, independently of the imposed initial rotation. This can become a problem in stellar modeling, since there are other factors that we do not take into account (e.g., magnetic braking, anisotropic winds, binary stars) that also have a great impact in the rotation, and that the α could possibly overpower.

The α parameter varying between 0.5 and 5 implies that the viscosity coefficient has to vary between 0.125 to 125 due to the cube dependence on α. Corresponding to a variation of 3 orders of magnitude both in the viscosity coefficient and in the required shear for the Tayler instability to saturate. Hence, the degree of freedom of this parameter is compensating for important missing physics not included in the Fuller-formalism, as discussed in previous reviews.

In early MS stages the core and surface rotation rates strongly depend on the initial rotation rate. The initial rotation period also has an impact in the model's age – lower initial periods seem to generate younger evolutionary tracks. Besides,

there is also a strong dependence of the viscosity on the local spin rate, $\nu_F \propto \Omega^3$ (Fuller et al. (2019)). As such, the fast track (left panel of Figure 7) in the early stages experiences a stronger decrease in rotation, although not enough to slow down the core to match the SGB measurements.

The surface rotation in not affected by the α parameter variations, on the other hand it highly depends on the rotation imposed at the ZAMS. Therefore, surface rotation rates in the left panel of Figure 7 do not match SGB and RGB measured rates, whereas the right panel of Figure 7 shows a better agreement with observations.

Our attempt to create a fast and slow rotation track to constraint the observed rotation rates, revealed that the Fuller-formalism overestimates the spin down of the core between the RGB and RC phase. We explored changing the α parameter after the RGB bump to compensate this effect, however it did not reproduce the desired results. Since most of the AM extraction in these models happens in the SGB and RGB. And at later stages, due to the large stabilizing composition gradients, the rotation rates are reproduced with conservation of AM (e.g., Cantiello et al. 2014, Fuller et al. 2019).

6. SUMMARY AND CONCLUSIONS

In the first part of this work, we concluded that the inner regions of evolved stars are mainly affected by diffusive transport processes. We performed side-by-side comparisons of four mechanisms of transport of AM that corroborated the small impact of different transport mechanisms in variables not related to rotation in RGB stars. We successfully reproduced the observed asteroseismic core rotation rate of a red giant star making use of a recently proposed mechanism based on the Tayler instability. The inherent calibration of the free parameter in this theory revealed a higher value than was initially proposed for RGB stars.

We implemented for the first time the rotational-driven mixing coefficient of the Fuller-formalism in the interior of RGB stars. Comparisons of the efficiency of three transport pro-

cesses revealed expected, albeit important results. The efficiency of mixing induced by rotation is overestimated in less efficient transport mechanisms due to higher core rotation predictions. Our study shows that the inclusion of mixing increases slightly the efficiency of AM transport.

Using the previous results, we carried out calculations for the oscillation mode frequencies. We verified the mixed mode period spacing pattern present in RGB stars. The period spacing and the frequency splitting of mixed modes showcased clear distinctions between different transport processes and small ones between mixing processes. This notable result confirms that asteroseismic derived rotational mixed mode split-

tings are a great tool to probe the values of the diffusion coefficient for AM transfer, and a potential tool to study the mixing of chemical elements in evolved stars.

Lastly, we performed a further study on the Fuller-formalism. Based on our results, the transport efficiency is particularly sensitive to variations on the initial stellar mass and less dependent on the metallicity and convective overshooting. With that information, we performed a calibration on the α parameter. Asteroseismic derived rotational splittings from a considerable amount of MS to RC stars were used to constraint the models. We established new limits for the α parameter of the Fuller-formalism using a wide range of rotators.

REFERENCES

Aerts, C., Christensen-Dalsgaard, J., Kurtz, D. W. 2010, (Springer)

Abolfathi, B., Aguado, D. S., Aguilar, G., et al. 2017, ApJS, 235, 42

Aguirre, V. S., Lund, M. N., Antia, H. M., et al. 2017, ApJ, 835, 2

Aerts, C., Mathis, S., Rogers, T. M. 2019, ARA&A, 57, 1, 35-78

Aerts, C. 2021, RvMP, 93, 1

Baglin, A., Auvergne, M., Barge, P., et al. 2007, AIP Conference Proceedings, 895, 1, 201-209

Borucki, W., Koch, D., Basri, G., et al. 2010, Science, 327, 977-80

Bedding, T. R., Huber, D., Stello, D. et al. 2010, ApJL, 713, 2, L176-L181

Bedding, T.R., Mosser, B., Huber, D., et al. 2011, Nature, 471, 7340, 608-611

Beck, P.G., Montalban, J., Kallinger, T., et al. 2012, Nature, 481, 7379, 55-57

Charbonnel, C., Talon, S. 2005, Science, 309, 5744, 2189-2191

Charbonnel, C., Lagarde, N. 2010, A&A, 522, A10

Chaplin, W. J., Miglio, A. 2013, ARA&A, 51, 1, 353-392

Cantiello, M., Mankovich, C., Bildsten, L., et al. 2014, ApJ, 788, 1, 93

Cunha, M. S., Stello, D., Avelino, P. P., et al. 2015, ApJ, 805, 2, 127

Dziembowski, W. A. 1971, AcA, 21, 289-306

Deheuvels, S., Dogan, G., Goupil, M. J., et al. 2014, A&A, 564, A27

den Hartogh, J. W., Eggenberger, P., Deheuvels, S. 2020, A&A, 634, L16

Endal, A. S., Sofia, S. 1978, ApJ, 220, 279-290

Eggenberger, P., Deheuvels, S., Miglio, A., et al. 2019a, A&A, 621, A66

Eggenberger, P., den Hartogh, J. W., Buldgen, G., et al. 2019c, A&A, 631, L6

Fuller, J., Piro, A. L., Jermyn, A. S. 2019, MNRAS, 485, 3, 3661-3680

Gilliland, R. L., Brown, T. M., Christensen-Dalsgaard, J., et al. 2010, PASP, 122, 888, 131-143

Gehan, C., Mosser, B., Michel, E., et al. 2018, A&A, 616, A24

Heger, A., Langer, N., Woosley, S. E., et al. 2000, ApJ, 528, 1, 368-396

Hekker, S., Christensen-Dalsgaard, J. 2017, A&A Rv, 25, 1

Hall, O. J., Davies, G. R, van Saders, J., et al. 2021, NatAs, 5, 7, 707-714

Koch, D. G., Borucki, W. J., Basri, G., et al. 2010, ApJ, 713, 2, L79-L86

Lagarde, N., Charbonnel, C., Decressin, T., et al. 2011, A&A, 536, A28

Meynet, G., Maeder, A. 1997, A&A, 321, 465-476

Maeder, A., Meynet, G. 2000, ARA&A, 38, 1, 143-190

Maeder, A., Meynet, G. 2004, A&A, 422, 1, 225-237

Mosser, B., Goupil, M. J., Belkacem, et al. 2012, A&A, 548, A10

Marques, J. P., Goupil, M. J., Lebreton, Y., et al. 2013, A&A, 549, A74

Nelder, J. A., Mead, R. 1965, CompJ, 7, 4, 308-313

Pitts, E. and Tayler, R. J. 1985, MNRAS, 216, 139-154

Paxton, B., Bildsten, L., Dotter, A., et al. 2011, ApJS, 192, 3

Paxton, B., Cantiello, M., Arras, P., et al. 2013, ApJS, 208, 4

Paxton, B., Marchant, P., Schwab, J., et al. 2015, ApJS, 220, 15

Paxton, B., Schwab, J., Bauer, E. B., et al. 2018, ApJS, 234, 34

Paxton, B., Smolec, R., Schwab, J. et al. 2019, ApJS, 243, 10

Pinsonneault, M. H., Elsworth, Y. P., Tayar, J., et al. 2018, ApJS, 239, 2

Ricker, G. R., Winn, J. N., Vanderspek, R., et al. 2014, JATIS, 1, 1, 014003

Rogers, T. M., Lin, D. N. C., McElwaine, J. N., et al. 2013, ApJ, 772, 1, 21

Rauer, H.,Catala, C., Aerts, C., et al. 2014, ExA, 249, 38

Shibahashi, H. 1979, PASJ, 31, 87-104

Spruit, H. C. 2002, A&A, 381, 3, 923-932

Somers, G., Pinsonneault, M. H. 2016, ApJ, 829, 1, 32

Tayler, R. J. 1973, MNRAS, 161, 365

Tassoul, M. 1980, ApJS, 43, 469-490

Townsend, R. H. D., Teitler, S. A. 2013, MNRAS, 435, 3406

Townsend, R. H. D., Goldstein, J., Zweibel, E. G. 2018, MNRAS, 475, 879

van Saders, J. L., Pinsonneault, M. H. 2013, ApJ, 776, 2, 67

Vrard, M. and Mosser, B. and Samadi, R. 2016, A&A, 588, A87

Zahn, J. P. 1992, A&A, 265, 115-132

Zahn, J.-P., Brun, A. S., Mathis, S. 2007, A&A, 474, 1, 145-154